

# Nanostructural and Electrochemical Evolution of the Solid-Electrolyte Interphase on CuO Nanowires Revealed by Cryogenic-Electron Microscopy and Impedance Spectroscopy

William Huang,<sup>†,||</sup> David T. Boyle,<sup>‡,||</sup> Yuzhang Li,<sup>†</sup> Yanbin Li,<sup>†</sup> Allen Pei,<sup>†</sup> Hao Chen,<sup>†</sup> and Yi Cui<sup>\*,†,§</sup>

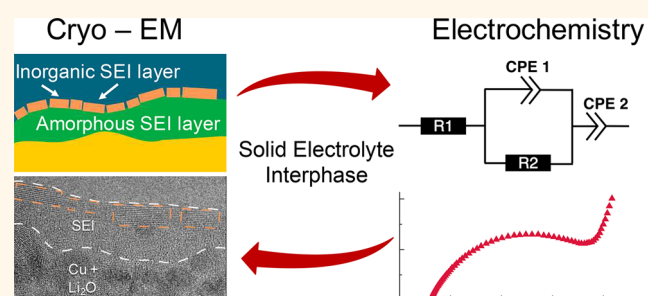
<sup>†</sup>Department of Materials Science and Engineering and <sup>‡</sup>Department of Chemistry, Stanford University, Stanford, California 94305, United States

<sup>§</sup>Stanford Institute for Materials and Energy Sciences, SLAC National Accelerator Laboratory, 2575 Sand Hill Road, Menlo Park, California 94025, United States

## Supporting Information

**ABSTRACT:** Battery performance is critically dependent on the nanostructure and electrochemical properties of the solid-electrolyte interphase (SEI)—a passivation film that exists on most lithium-battery anodes. However, knowledge of how the SEI nanostructure forms and its impact on ionic transport remains limited due to its sensitivity to transmission electron microscopy and difficulty in accurately probing the SEI impedance. Here, we track the voltage-dependent, stepwise evolution of the nanostructure and impedance of the SEI on CuO nanowires using cryogenic-electron microscopy (cryo-EM) and electrochemical impedance spectroscopy (EIS). In carbonate electrolyte, the SEI forms at 1.0 V vs Li/Li<sup>+</sup> as a 3 nm thick amorphous SEI and grows to 4 nm at 0.5 V; as the potential approaches 0.0 V vs Li/Li<sup>+</sup>, the SEI on the CuO nanowires forms an 8 nm thick inverted multilayered nanostructure in ethylene carbonate/diethyl carbonate (EC/DEC) electrolyte with 10 vol % fluoroethylene carbonate (FEC) and a mosaic nanostructure in EC/DEC electrolyte. Upon Li deposition, the total SEI thickness grows to 16 nm, and significant growth of the inner amorphous layer takes place in the inverted multilayered nanostructure, indicating that electrolyte permeates the SEI. Using a refined EIS methodology, we isolate the SEI impedance on Cu and find that the SEI nanostructure directly correlates to macroscopic Li-ion transport through the SEI. The inverted layered nanostructure decreases the interfacial impedance upon formation, whereas the mosaic nanostructure continually increases the interfacial impedance during growth. These structural and electrochemical findings illustrate a more complete portrait of SEI formation and guide further improvements in engineered SEI.

**KEYWORDS:** batteries, transmission electron microscopy, cryogenic-electron microscopy, solid-electrolyte interphase, lithium-ion batteries, lithium-metal anode



Understanding the intimate nanoscale features of high-energy battery materials and their impact on the electrochemical properties of a cell is critical for their successful deployment. Of paramount importance is the solid-electrolyte interphase (SEI), a surface passivation film that forms on all lithium (Li)-battery anodes.<sup>1–3</sup> The SEI is requisite to the operation of the battery; it both stabilizes the reductive anode in the electrolyte environment and mediates Li-ion transfer from electrolyte to the electrode. However, Li and electrolyte are consumed during the formation of the SEI, which results in capacity fade of Li-based batteries.<sup>4,5</sup> The realization of higher energy density battery chemistries

necessitates a comprehensive understanding of the structural, chemical, and electrochemical properties of the SEI, but this goal has remained elusive.

Toward this aim, numerous studies have characterized the chemical and electrochemical properties of the SEI on various anode materials.<sup>6–8</sup> However, elucidation of the SEI nanostructure has been difficult because of the reactivity and

**Received:** October 19, 2018

**Accepted:** December 27, 2018

**Published:** December 27, 2018

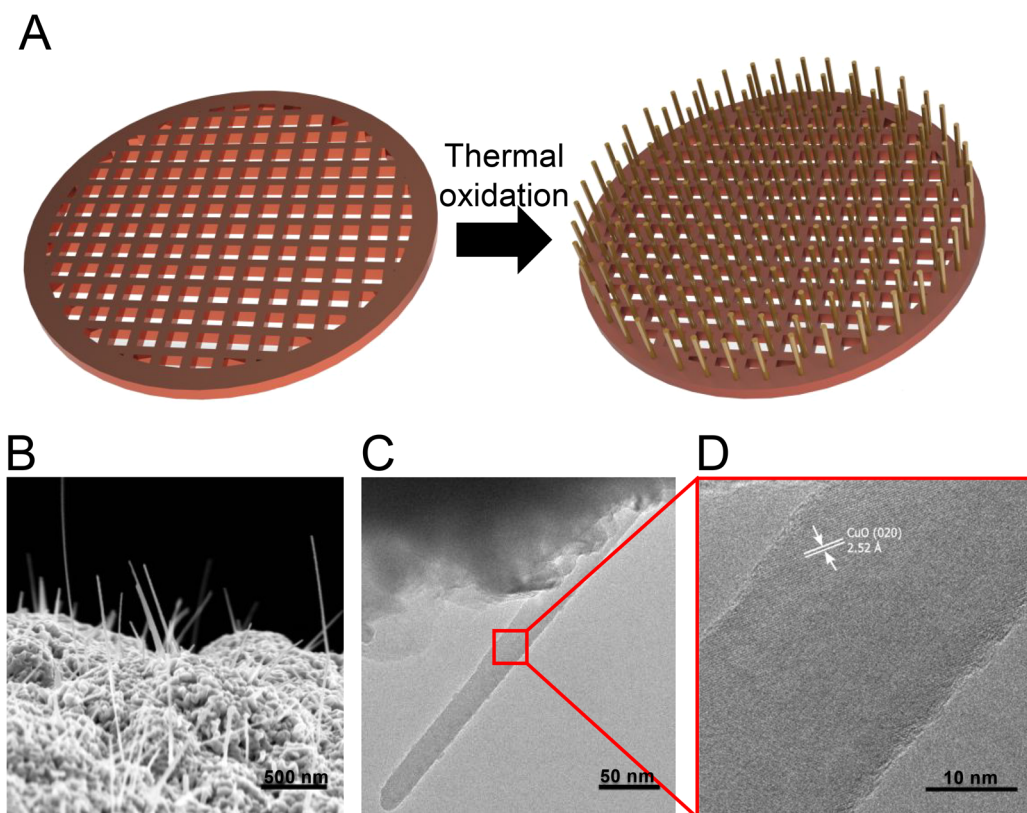


**Figure 1.** Schematic of CuO nanowire synthesis. (A) Oxidation of a Cu TEM grid results in an array of CuO NWs. (B) SEM and (C,D) TEM characterization of CuO nanowires as synthesized.

sensitivity of many battery materials and interphases to transmission electron microscopy (TEM) and air. Recent advances in cryogenic-electron microscopy (cryo-EM) stabilized the metallic Li anode and its SEI in the TEM, so high-resolution imaging of both phases and their interface could be achieved. Two distinct SEI nanostructures were found in two different carbonate electrolytes.<sup>9</sup> Similar to the mosaic model originally proposed by Peled, the SEI on Li in 1:1 ethylene carbonate/diethylene carbonate (EC/DEC) electrolyte was composed of inorganic, nanocrystalline grains of  $\text{Li}_2\text{O}$  and  $\text{Li}_2\text{CO}_3$  embedded within a matrix of amorphous material.<sup>10,11</sup> When 10 vol % of fluoroethylene carbonate (FEC) was added to the EC/DEC electrolyte, the SEI had a distinct inverted layered structure. The inner layer of the SEI consisted of an amorphous layer of material, while an inorganic, crystalline layer of  $\text{Li}_2\text{O}$  formed the outer layer, similar to the model proposed by Aurbach but with an inverted layer sequence.<sup>6</sup> Through cryo-EM, the functional effects of these nanostructures have been elucidated, and the SEI nanostructure played a significant role in the performance of different battery systems. Specifically, the inverted layered SEI nanostructure homogenized  $\text{Li}^+$ -ion transport and resulted in high cycling performance of Li-metal anodes, whereas the mosaic nanostructure had irregular  $\text{Li}^+$  flux and led to significant cycling inefficiency.<sup>12</sup>

One of the important remaining questions is how the SEI evolves both structurally and electrochemically upon the voltage change during the first charging cycle of batteries. Previous characterizations of SEI formation on relevant, inert substrates such as Cu using methods such as X-ray photoelectron spectroscopy, time-of-flight secondary-ion mass spectrometry, Fourier-transform infrared spectroscopy, atomic force microscopy, and small-angle X-ray scattering have been

unable to directly observe the evolution of the SEI nanostructure.<sup>13–17</sup> Additionally, the electrochemical formation of SEI on inert substances has been studied with electrochemical impedance spectroscopy (EIS),<sup>15,18</sup> but the cell geometries and high-impedance reference/counter electrodes used in previous studies make the interpretation of the EIS results unclear. Many three-electrode cell geometries introduce artifacts into the data, and high-impedance counter/reference electrodes, such as Li, inadequately isolate the EIS response of the SEI alone.<sup>19–21</sup>

Here, we study the nanostructural and electrochemical evolution pathway of a model SEI on a Cu current collector with cryo-EM and EIS. Cryo-EM reveals the nanostructural evolution of SEI in carbonate electrolyte systems as the Cu electrode is systematically lowered in potential to 0 V vs Li/Li<sup>+</sup>, while a refined EIS method isolates the impedance of the model SEI at each step during formation. We directly correlate the nanostructures of SEI to electrochemical impedance. These insights further guide efforts in rationally engineering functional SEI for next-generation battery chemistries.

## RESULTS/DISCUSSION

**Growth of CuO NWs on a TEM Grid.** TEM necessitates electron transparent specimens; however, conventional processing methods for TEM imaging such as focused-ion beam (FIB) or microtomy risk introducing chemical or mechanical artifacts.<sup>22</sup> In order to observe the SEI in its pristine state with minimal processing, we grow SEI directly on a TEM grid. The oxidation of a Cu TEM grid offers a facile route to CuO nanowires (NWs) for use as an imaging substrate to probe the electrode–electrolyte interface. Although Cu foil is commonly

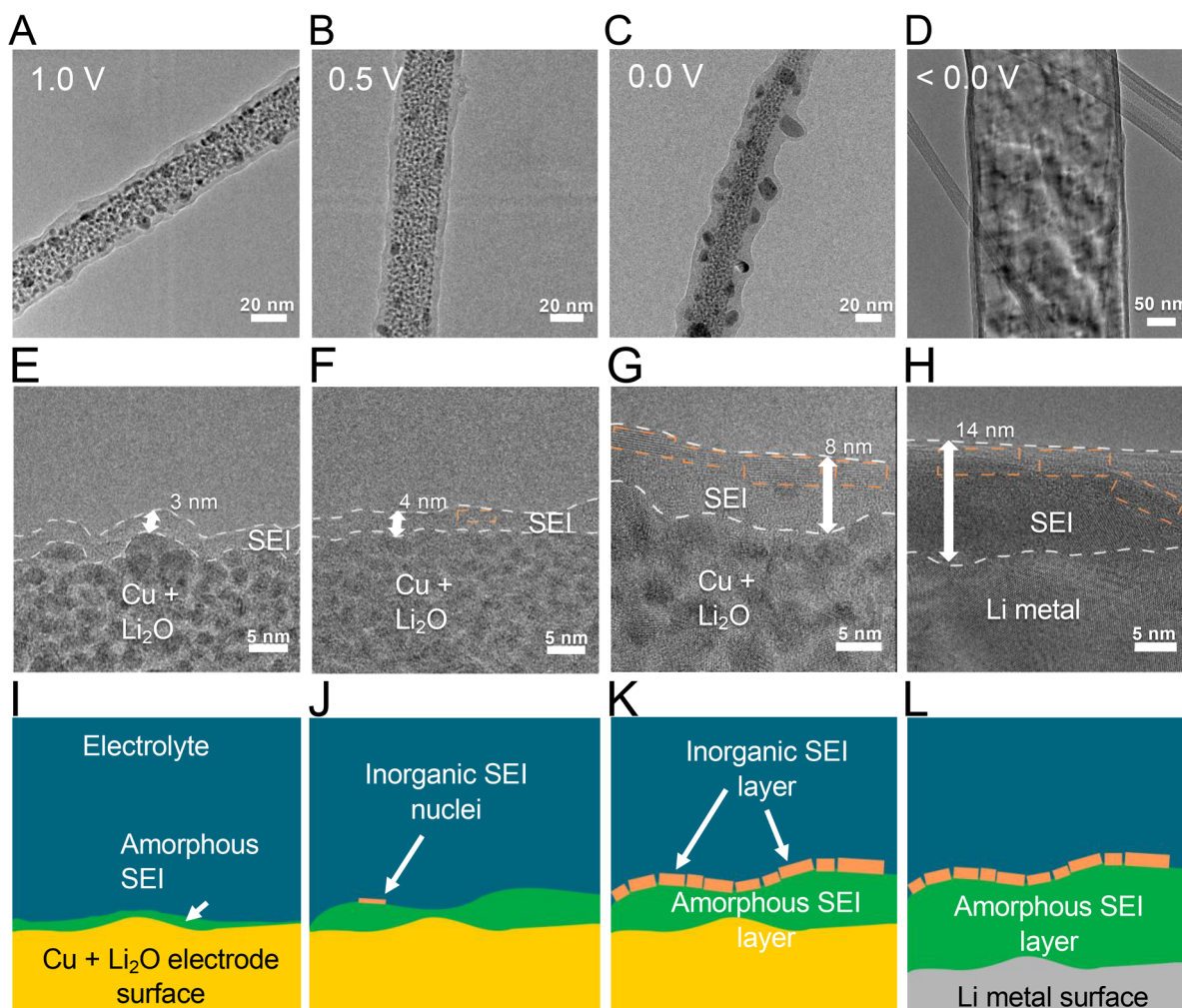


**Figure 2.** Structural evolution of the inverted layered SEI nanostructure in EC/DEC + 10% FEC electrolyte. (A–D) Low-magnification and (E–H) high-magnification images of the SEI formed on CuO at different potentials and Li metal. (I–L) Illustrations depicting the evolution of the nascent SEI from 1.0 V vs Li/Li<sup>+</sup> to Li deposition. Larger versions of the TEM images are included in the [Supporting Information](#).

used as the Li electrodeposition substrate in Cu||Li half-cells<sup>23</sup> and anode-free lithium-metal batteries,<sup>24</sup> the native oxide of Cu is always present on the surface, and the true electrode–electrolyte interface is CuO coupled with liquid electrolyte.<sup>25–27</sup> CuO NWs can be easily synthesized through the thermal oxidation of Cu,<sup>28,29</sup> illustrated in [Figure 1A](#). The oxidation of a Cu TEM grid results in CuO NWs grown normal to the substrate, which is subsequently assembled into a coin-cell. SEM ([Figure 1B](#)) and TEM ([Figure 1C,D](#)) characterization of the CuO NW TEM grid shows dense arrays of single crystalline CuO nanowires with diameters of 30 nm and lengths up to 1  $\mu\text{m}$ . When used as the working electrode in a Li/Cu half-cell, CuO NWs model the electrode–electrolyte interface while being electron transparent and allow direct imaging of the electrode surface at different potentials.

**Electrochemical Reduction of EC/DEC with 10% FEC Electrolyte on CuO NW.** We assembled a CuO NW TEM grid||Li half-cell to track the formation and structural evolution of the SEI in carbonate electrolyte systems at varying potentials using cryo-EM. We carried out experiments in EC/DEC electrolyte with 10 vol % FEC, which exhibits improved cycling stability compared to EC/DEC and is an illustrative system because of its distinct inverted layered SEI nanostructure. The CuO nanowire TEM grids are galvanostatically discharged to

varying potentials vs Li/Li<sup>+</sup> and held at that potential for 8 h to ensure complete SEI formation ([Figure S1](#)). CuO undergoes a conversion reaction at 1.0 V vs Li/Li<sup>+</sup>,<sup>30–32</sup> forming Cu and Li<sub>2</sub>O and resulting in a polycrystalline Cu/Li<sub>2</sub>O NW ([Figure 2A,E](#)). The smooth surface of the CuO NW ([Figure 1C](#)) roughens during the conversion reaction ([Figure 2A](#)) as CuO segregates into grains of Cu and Li<sub>2</sub>O during lithiation. These observations indicate that the CuO–electrolyte interface is no longer present below 1.0 V vs Li/Li<sup>+</sup>; the initial CuO electrode surface instead restructures to form nanocrystalline Cu and Li<sub>2</sub>O. This indicates that Li nucleation on Cu takes place on a heterogeneous, rough substrate regardless of the initial flatness of the oxidized substrate, which is important for fundamental studies of Li growth on Cu<sup>23</sup> along with anodeless Li-metal batteries.<sup>24</sup> Following conversion of the CuO electrode surface into Cu and Li<sub>2</sub>O, a thin SEI with an average thickness of 3 nm ([Figure S2](#)) can be observed coating the Cu/Li<sub>2</sub>O NW at 1.0 V ([Figure 2A,E](#)). This SEI is amorphous and primarily composed of carbon and oxygen, as indicated by energy filtered TEM (EFTEM) mapping ([Figure S3](#)) and electron energy loss spectroscopy (EELS) ([Figure S4](#)). Reducing the potential further to 0.5 V vs Li/Li<sup>+</sup>, the SEI continues to grow and thicken to an average of 4 nm with small, dilute grains of crystalline SEI components beginning to nucleate ([Figure](#)

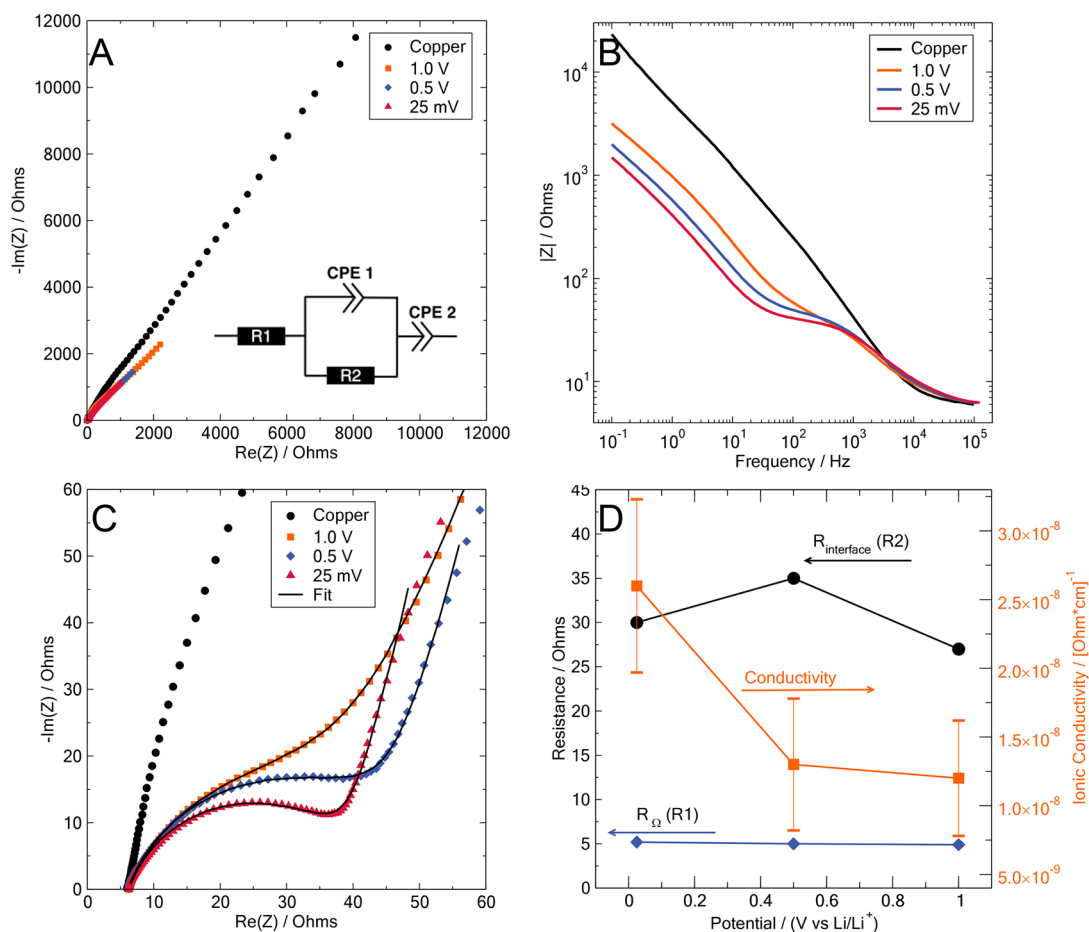


**Figure 3.** Impedance evolution of the inverted layered SEI nanostructure in EC/DEC + 10% FEC electrolyte. (A) Nyquist representation of the impedance of an LTO || Cu cell prior to the growth of SEI and of SEI growth at 1.0, 0.5, and 0.025 V vs Li/Li<sup>+</sup>. (B) Bode representation. (C) Zoomed in section of (A) showing the impedance of the SEI as a function of the potential. The equivalent circuit model used to fit each curve is shown in the inset of (A). (D) The  $R_{\Omega}$ ,  $R_{\text{interface}}$ , and ionic conductivity of the SEI as a function of potential. Error bars account for the standard deviation of the SEI thickness.

2B,F). The nascent inorganic grains of SEI nuclei are spatially consistent with the inverted layered nanostructure, with crystalline components precipitating at the outer interface of the SEI.

As the working electrode potential is brought to the same electrochemical potential as the Li counter electrode (0.0 V vs Li/Li<sup>+</sup>), electrolyte molecules further decompose, and the inverted layered (Figure 2C,G) SEI nanostructure emerges on the Cu electrode surface. The electrochemically formed SEI on Cu/Li<sub>2</sub>O grows significantly when the potential is reduced to 0.0 V. The thickness of the SEI increases to an average of 8 nm and forms the characteristic inverted layered structure with crystalline Li<sub>2</sub>O/Li<sub>2</sub>CO<sub>3</sub> interfaced with an inner amorphous layer. Recent work showed that agglomerates of LiF nanoparticles precipitate onto anodes in similar carbonate electrolytes, rather than growing within the primary SEI nanostructure.<sup>33</sup> The cryo-EM data reported here focuses on the primary SEI in direct contact with the electrode, which does not show any appreciable amount of crystalline LiF. Evidently, the nanostructure of the SEI arises from the stepwise decomposition of electrolyte molecules and is fully developed at 0.0 V vs Li/Li<sup>+</sup>. These observations confirm that the SEI nanostructure emerges purely through electrochemical decomposition of electrolyte and exists in electrochemical systems operating at potentials close to, but above, Li deposition.

Li metal electrodeposits when the potential of the electrode is further reduced to a negative overpotential below 0.0 V vs Li/Li<sup>+</sup>.<sup>23</sup> Figure 2D,H shows Li metal grown in EC/DEC + 10% FEC electrolyte systems on standard Cu foil and its characteristic inverted layered nanostructure. Strikingly, the SEI thickens considerably on the surface of Li metal: 8 nm at 0.0 V on the NW to 16 nm on electrodeposited Li. This thickness evolution implies that further SEI growth takes place beyond the electrochemical formation of SEI at 0.0 V because of chemical reactions between Li and electrolyte and continued electrochemical decomposition of electrolyte as a result of the Li deposition overpotential. Furthermore, significant growth takes place in the amorphous component of the SEI. This indicates that the continued growth of SEI below 0.0 V does not necessarily occur at the electrolyte/SEI interface, but rather below the inorganic SEI layer. For this to be the case, solvent molecules must enter the SEI by diffusion through the inorganic Li<sub>2</sub>O/Li<sub>2</sub>CO<sub>3</sub> surface layer and subsequently be reduced at the anode. This comparison of SEI thickness at 0.0 V and below 0.0 V illustrates that the SEI is not impenetrable to electrolyte, but portions of the SEI are swollen or permeable to electrolyte.

**Impedance Response of Inverted Layered SEI Nanostructure on Cu with EC/DEC and 10% FEC.** Such drastic nanostructural changes in the SEI should directly

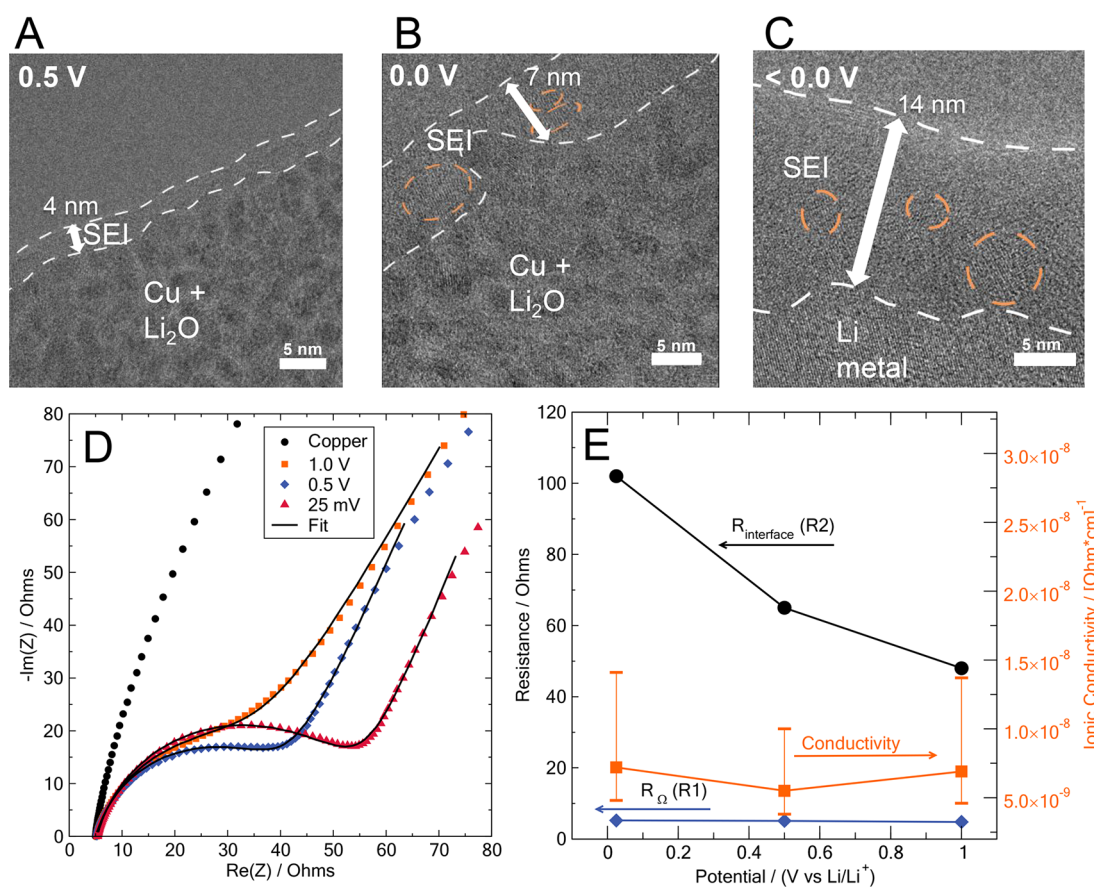


**Figure 4.** Structural and electrochemical evolution of the mosaic SEI nanostructure in EC/DEC electrolyte. (A) SEI formed at 0.5 V vs Li/Li<sup>+</sup>. (B) SEI formed at 0.0 V. (C) SEI formed on Li metal. (D) Impedance of the SEI in EC/DEC. (E) SEI resistance and corresponding conductivity. Larger versions of the TEM images are included in the [Supporting Information](#).

correlate to Li-ion transport through the interphase. Previous works have measured the impedance response of an SEI grown on Cu using a Li||Cu coin-cell geometry,<sup>15</sup> but using the same Li electrode as both the counter and reference electrode makes EIS data unclear. The impedance of the Li counter electrode—normalized to the geometric electrode surface area—is on the same order of magnitude as the impedance in Li||Cu EIS measurements (Figure S5). Since the total impedance is a sum of the impedance from each electrode,<sup>34</sup> it is impractical to deconvolute the contribution of Li from the SEI on Cu. Additionally, the impedance of a Li electrode increases with time because of continuous reaction with the electrolyte, further complicating the EIS interpretation (Figure S6). A three-electrode cell could isolate the impedance response of a single electrode, but three-electrode cell geometries for Li batteries generally have electrochemical and geometrical asymmetries within the cell.<sup>19–21,35</sup> These asymmetries result in an inhomogeneous current density near the reference electrode, which produces distortions in the impedance spectra.<sup>20</sup> Therefore, it is necessary to refine the impedance measurement of two-electrode cells to be dominated by the working electrode of interest.

In order to accurately measure the impedance of the SEI on Cu foil and decouple the working electrode impedance from that of the counter/reference electrode, we use pre-cycled and half-charged Li<sub>4</sub>Ti<sub>5</sub>O<sub>12</sub>/Li<sub>7</sub>Ti<sub>5</sub>O<sub>12</sub> (LTO) as the counter/reference electrode in a two-electrode, coin-cell geometry. LTO has a stable potential (1.567 V vs Li/Li<sup>+</sup>) in nonaqueous

electrolyte, and the interfacial impedance of the LTO electrode is 2 orders of magnitude smaller than that of lithium<sup>34</sup> (Figure S7A,B). The impedance of an LTO||Li coin-cell is nearly identical in magnitude, shape, and frequency response to the normalized impedance of Li (Figure S7C). As a result, LTO will allow us to isolate the impedance response of the SEI on Cu in a two-electrode cell.

Immediately after assembly of the LTO||Cu half-cells in EC/DEC + 10 vol % FEC electrolyte, the impedance is measured to obtain the control response of a pristine copper electrode (Figure 3A). The cell is then galvanostatically discharged to 1.0, 0.5, and 0.025 V vs Li/Li<sup>+</sup>, similar to our cryo-EM procedure (Figure S8). The results of the EIS measurements are shown in Figure 3A–D and fit to the equivalent circuit shown in Figure 3A. The circuit includes a resistor for the resistance of the electrolyte (R1), a resistor (R2) in parallel to a constant phase element (CPE1) to represent the interfacial impedance of the SEI and the dielectric response of the SEI, respectively, and a CPE to represent the SEI–Cu interface (CPE2). Results of the equivalent circuit fit for each EIS measurement are shown in the Supporting Information (Tables S1 and S2).

The impedance response of SEI on Cu in Li-based cells spans several orders of magnitude in frequency and Z (Ohms), so analysis of the spectra is separated into three regions. First, we consider the highest frequency range (10–100 kHz) where the electrolyte resistance dominates the impedance. The series resistance (R1) increases very slightly as the Cu potential is

reduced from the open-circuit voltage (OCV) to 0 V (Figure 3D and Table S1). This relatively constant series resistance at each potential is expected, as only small amounts of electrolyte react with the surface.

The impedance of the SEI manifests itself in midrange frequencies: from 0.1–1 kHz. On the pristine Cu, the impedance response is primarily capacitive from charge accumulation on the Cu electrode. Once the potential of Cu is lowered to 1.0 V, a depressed semicircle, the characteristic response of an SEI, is observed in the impedance (Figure 3C). Interestingly, the ionic resistance of the SEI ( $R_2$ ) increases when the potential is lowered from 1.0 to 0.5 V but subsequently decreases from 0.5 to 0.025 V (Figure 3C,D). In order to understand how the intrinsic electrochemical properties of the SEI evolve, the interfacial resistance ( $R_2$ ) is converted to an average ionic conductivity of the SEI (Figure 3D, orange curve). Interestingly, as the potential of Cu approaches 0 V, the SEI thickness increases (Figure 2E–H), but the average ionic conductivity trends upward. The increasing ionic conductivity of the SEI may be a result of the emergence of the outer layer of nanocrystalline  $\text{Li}_2\text{O}$ . Although bulk  $\text{Li}_2\text{O}$  is an ionic insulator, the nanoscopic dimensions of the  $\text{Li}_2\text{O}$  grains may facilitate a Lewis-acid transport mechanism of Li-ions through the oxide layer.<sup>36,37</sup> The lower resistivity could also be attributed to a denser and ionically conductive amorphous layer in the SEI that is formed at lower potentials.<sup>38</sup>

Lastly, we investigate the low-frequency component of the impedance response (1–0.2 Hz), which receives little attention in previous reports.<sup>15,18</sup> At these frequencies, the diffusion of ions and charge accumulation on the Cu electrode dominates (CPE 2). The bare Cu electrode exhibits a capacitive response at low frequencies (Figure 3A,B). As the potential of the Cu electrode is lowered toward 0.0 V vs Li/Li<sup>+</sup>, the low-frequency impedance decreases (Figure 3A,B). The impedance is attributed to the diffusion of ions through the SEI to the Cu electrode where the ions then accumulate at the SEI–Cu interface. These results are expected because of the lower resistivity of the SEI at lower potentials as discussed above. Ultimately, we find that the thickness of the SEI is not the dominant factor; the increasing ionic conductivity at low potentials illustrates that the SEI nanostructure is the dominant factor in Li-ion transport through the SEI.

#### Cryo-EM and EIS Characterization of the EC/DEC SEI.

To compare how different SEI nanostructures influence the properties of the SEI, we carried out similar analyses for an SEI grown in EC/DEC without FEC additives. Cryo-EM characterization of the SEI formed on CuO NWs in EC/DEC shows that it forms the mosaic nanostructure rather than the inverted layered nanostructure seen in EC/DEC + 10 vol % FEC (Figure 4A–C). Similar to the case of EC/DEC with 10% FEC, the SEI in EC/DEC emerges at 1.0 V with an average thickness of 3 nm and further grows to an average of 7 nm at 0.0 V vs Li/Li<sup>+</sup>. The SEI nanostructure is fully formed at 0.0 V and thickens further to 16 nm as Li metal is deposited. Interestingly, EIS characterization of the nascent SEI shows that the impedance still correlates strongly with potential (Figure 4D); however, rather than a decreased impedance with decreasing potential observed in the inverted layered system, the EC/DEC SEI exhibits a continuously increasing impedance and relatively constant ionic conductivity as the potential is reduced (Figure 4E). Additionally, the ionic conductivity of the SEI in EC/DEC is less than the ionic

conductivity of the SEI in EC/DEC + 10% FEC (Figures 3D and 4E). The emergence of inorganic grains within the SEI and/or a generally thicker amorphous layer may lead to a higher ionic resistivity in the EC/DEC system.

## CONCLUSION

We image the stepwise evolution of the SEI nanostructure on oxidized Cu with cryo-EM and couple our structural observations to EIS, which elucidates the strong influence of SEI nanostructure on Li-ion transport. CuO NW TEM grids afford fundamental insights into the structural evolution of SEI nanostructure on Cu electrodes. In carbonate electrolytes, we observe a nascent amorphous SEI formed as the initially smooth CuO electrode surface is lithiated and restructured into rough Cu and  $\text{Li}_2\text{O}$  nanograins. The SEI then grows crystalline SEI components at potentials below 0.5 V vs Li/Li<sup>+</sup>. As potentials approach 0.0 V vs Li/Li<sup>+</sup>, the SEI nanostructure is fully formed solely through electrochemical electrolyte decomposition and further grows when Li metal is deposited. In inverted layered systems, we observe that SEI growth occurs underneath the inorganic outer layer, indicative of electrolyte penetration into the nascent SEI. We correlate these observations to the impedance of the SEI and find that the ionic conductivity of the SEI changes dramatically with decreasing potentials, which illustrates the influence of the nanostructure on its ionic transport characteristics. The acuity gleaned from this study of SEI growth on Cu paints a more complete picture of electrochemical SEI formation, which will be critical for development of rationally designed SEI through electrolyte engineering.

## METHODS

**CuO Nanowire Synthesis.** Cu TEM grids were oxidized in a tube furnace at 300 °C for 30 min in ambient air.

#### Electrochemical Formation of SEI and Cu/Li<sub>2</sub>O Nanowires.

Type 2032 coin-cells were assembled in an argon glovebox with a polymer separator (Celgard 2250), Li-metal foil (Alfa Aesar) as the counter/reference electrode, and Cu foil with an oxidized TEM grid placed in the center as the working electrode. The electrolyte used was 1.0 M LiPF<sub>6</sub> in 1:1 w/w ethylene carbonate/diethyl carbonate (BASF Selectilyte LP40). In studies with FEC electrolyte additive, 1.0 M LiPF<sub>6</sub> in 90 vol % 1:1 v/v ethylene carbonate/diethyl carbonate and 10 vol % fluoroethylene carbonate (Novolyte Technologies Inc.) was used. In all cases, cells were assembled with 75  $\mu\text{L}$  of electrolyte.

CuO reduction and SEI formation were carried out at a positive areal current density of 50  $\mu\text{A cm}^{-2}$  using a 96-channel Arbin battery tester. After the voltage of interest was reached, the cell was maintained at that voltage for 8 h before disassembly. For Li-metal deposition, a positive areal current density of 2.0 mA  $\text{cm}^{-2}$  was applied for 30 min, resulting in an areal capacity of 1.0 mAh  $\text{cm}^{-2}$  (Figure S1). No TEM grid was placed in the cell; Li was deposited directly on the Cu foil. Li metal was removed from the foil and cast onto a lacey carbon TEM grid for cryogenic preparation and imaging.

**Cryogenic Sample Preparation.** The batteries were disassembled in an argon-filled glovebox and rinsed with 1,3-dioxolane (DOL) to remove Li salts. Our rinsing procedure attempts to minimize artifacts by using minimal force and solvent volume; approximately 100  $\mu\text{L}$  is carefully dropped onto the TEM grid after the battery is disassembled. Immediately after rinsing, the sample is transferred into liquid nitrogen outside the glovebox using a sealed container. While immersed in liquid nitrogen, the sample is loaded into the cryo-EM holder and inserted into the TEM column. The cryo-EM holder uses a specialized shutter to prevent air exposure and condensation onto the sample, which preserves the specimen in its native state.

**Electron Microscopy.** All cryo TEM characterizations were carried out using an FEI Titan 80-300 environmental (scanning) transmission electron microscope operated at an accelerating voltage of 300 kV. The instrument is equipped with an aberration corrector in the objective lens, which was tuned before each sample analysis. Conventional TEM images were obtained using an FEI Tecnai G2 F20 X-TWIN (scanning) transmission electron microscope at an accelerating voltage of 200 kV. Lattice spacings of  $\text{Li}_2\text{O}$ , Cu, and  $\text{CuO}$  were analyzed using Gatan Digital Micrograph software (Figure S9). SEM characterization was carried out using a FEI Magellan 400 XHR scanning electron microscope. Measurements of the SEI thickness at each potential were taken from many TEM images, and the average values were reported in the main text.

**Electrochemical Impedance Spectroscopy.** A slurry containing 80% LTO, 10% carbon-black, super-P, 7% carboxymethyl cellulose binder, and 3% styrene-butadiene rubber in water was used for the LTO electrodes. The LTO slurry was cast onto aluminum foil with a loading of approximately  $1 \text{ mAh/cm}^2$ . The LTO is cycled in a Li||LTO cell twice before charging the LTO to half of its total capacity. The copper was thoroughly rinsed with deionized water, acetone, and then isopropanol and pumped into a glovebox prior to assembly of LTO||Cu coin-cells. Type 2032 coin-cells and Celgard 2250 separators were used in each EIS experiment. Immediately after assembly of the coin-cells, the impedance of the LTO||Cu coin-cell is measured to obtain the control response of the copper. After EIS, the Cu is galvanostatically discharged to  $-0.567 \text{ V}$  vs LTO ( $1.0 \text{ V}$  vs  $\text{Li/Li}^+$ ) with a current density of  $50 \mu\text{A cm}^{-2}$ . Once the potential of the copper reaches  $-0.567 \text{ V}$  vs LTO, the potential is held until the measured current density is  $<1 \mu\text{A cm}^{-2}$ . At this point, the cell rests for 30 min to relax any double layer charging, and EIS is taken at OCV. The discharge and EIS procedure are repeated for  $-1.067 \text{ V}$  vs LTO and  $-1.542 \text{ V}$  vs LTO ( $0.5$  and  $0.025 \text{ V}$  vs  $\text{Li/Li}^+$ ). The same channel, clamp, and wires were used throughout each measurement.

## ASSOCIATED CONTENT

### Supporting Information

The Supporting Information is available free of charge on the ACS Publications website at DOI: 10.1021/acsnano.8b08012.

Supporting figures and tables as described in the text (PDF)

## AUTHOR INFORMATION

### Corresponding Author

\*E-mail: [yicui@stanford.edu](mailto:yicui@stanford.edu).

### ORCID

William Huang: 0000-0001-8717-5337

David T. Boyle: 0000-0002-0452-275X

Yuzhang Li: 0000-0002-1502-7869

Yanbin Li: 0000-0002-5285-8602

Allen Pei: 0000-0001-8930-2125

Hao Chen: 0000-0002-2852-0070

Yi Cui: 0000-0002-6103-6352

### Author Contributions

<sup>||</sup>W.H. and D.T.B. contributed equally.

### Notes

The authors declare no competing financial interest.

## ACKNOWLEDGMENTS

The authors acknowledge L. Dang for graphic design input. D.T.B. and Yuzhang Li acknowledge the National Science Foundation Graduate Research Fellowship Program (NSF GRFP) for funding. A.P. acknowledges the support from Stanford University through the Stanford Graduate Fellowship

(SGF) Program. Y.C. acknowledges the support from the Assistant Secretary for Energy Efficiency and Renewable Energy, Office of Vehicle Technologies of the U.S. Department of Energy under the Battery Materials Research (BMR) Program and Battery 500 Consortium Programs. Part of this work was performed at the Stanford Nano Shared Facilities (SNSF), supported by the National Science Foundation under award ECCS-1542152.

## REFERENCES

- (1) Peled, E.; Menkin, S. Review—SEI: Past, Present and Future. *J. Electrochem. Soc.* **2017**, *164*, A1703–A1719.
- (2) Verma, P.; Maire, P.; Novák, P. A Review of the Features and Analyses of the Solid Electrolyte Interphase in Li-Ion Batteries. *Electrochim. Acta* **2010**, *55*, 6332–6341.
- (3) Cheng, X. B.; Zhang, R.; Zhao, C. Z.; Wei, F.; Zhang, J. G.; Zhang, Q. A Review of Solid Electrolyte Interphases on Lithium Metal Anode. *Adv. Sci.* **2016**, *3*, 1500213.
- (4) Pinson, M. B.; Bazant, M. Z. Theory of SEI Formation in Rechargeable Batteries: Capacity Fade, Accelerated Aging and Lifetime Prediction. *J. Electrochem. Soc.* **2013**, *160*, A243–A250.
- (5) Aurbach, D.; Zinigrad, E.; Cohen, Y.; Teller, H. A Short Review of Failure Mechanisms of Lithium Metal and Lithiated Graphite Anodes in Liquid Electrolyte Solutions. *Solid State Ionics* **2002**, *148*, 405–416.
- (6) Aurbach, D. The Surface Chemistry of Lithium Electrodes in Alkyl Carbonate Solutions. *J. Electrochem. Soc.* **1994**, *141*, L1–L3.
- (7) Eshkenazi, V.; Peled, E.; Burstein, L.; Golodnitsky, D. XPS Analysis of the SEI Formed on Carbonaceous Materials. *Solid State Ionics* **2004**, *170*, 83–91.
- (8) Nie, M.; Abraham, D. P.; Chen, Y.; Bose, A.; Lucht, B. L. Silicon Solid Electrolyte Interphase (SEI) of Lithium Ion Battery Characterized by Microscopy and Spectroscopy. *J. Phys. Chem. C* **2013**, *117*, 13403–13412.
- (9) Li, Y.; Li, Y.; Pei, A.; Yan, K.; Sun, Y.; Wu, C.-L.; Joubert, L.-M.; Chin, R.; Koh, A. L.; Yu, Y.; et al. Atomic Structure of Sensitive Battery Materials and Interfaces Revealed by Cryo – Electron Microscopy. *Science* **2017**, *358*, 506–510.
- (10) Peled, E. The Electrochemical Behavior of Alkali and Alkaline Earth Metals in Nonaqueous Battery Systems—The Solid Electrolyte Interphase Model. *J. Electrochem. Soc.* **1979**, *126*, 2047.
- (11) Peled, E. Advanced Model for Solid Electrolyte Interphase Electrodes in Liquid and Polymer Electrolytes. *J. Electrochem. Soc.* **1997**, *144*, L208.
- (12) Li, Y.; Huang, W.; Li, Y.; Pei, A.; Boyle, D. T.; Cui, Y. Correlating Structure and Function of Battery Interphases at Atomic Resolution Using Cryo-Electron Microscopy. *Joule* **2018**, *2*, 2167.
- (13) Owejan, J. E.; Owejan, J. P.; Decaluwe, S. C.; Dura, J. A. Solid Electrolyte Interphase in Li-Ion Batteries: Evolving Structures Measured *in Situ* by Neutron Reflectometry. *Chem. Mater.* **2012**, *24*, 2133–2140.
- (14) Bülter, H.; Peters, F.; Schwenzel, J.; Wittstock, G. Spatiotemporal Changes of the Solid Electrolyte Interphase in Lithium-Ion Batteries Detected by Scanning Electrochemical Microscopy. *Angew. Chem., Int. Ed.* **2014**, *53*, 10531–10535.
- (15) Lu, P.; Li, C.; Schneider, E. W.; Harris, S. J. Chemistry, Impedance, and Morphology Evolution in Solid Electrolyte Interphase Films during Formation in Lithium Ion Batteries. *J. Phys. Chem. C* **2014**, *118*, 896–903.
- (16) Zhuo, Z.; Lu, P.; Delacourt, C.; Qiao, R.; Xu, K.; Pan, F.; Harris, S. J.; Yang, W. Breathing and Oscillating Growth of Solid-Electrolyte-Interphase upon Electrochemical Cycling. *Chem. Commun.* **2018**, *54*, 814–817.
- (17) Lu, P.; Harris, S. J. Lithium Transport within the Solid Electrolyte Interphase. *Electrochem. Commun.* **2011**, *13*, 1035–1037.
- (18) Zaban, A.; Aurbach, D. Impedance Spectroscopy of Lithium and Nickel Electrodes in Propylene Carbonate Solutions of Different

Lithium Salts A Comparative Study. *J. Power Sources* **1995**, *54*, 289–295.

(19) Costard, J.; Ender, M.; Weiss, M.; Ivers-Tiffée, E. Three-Electrode Setups for Lithium-Ion Batteries. *J. Electrochem. Soc.* **2017**, *164*, A80–A87.

(20) Ender, M.; Illig, J.; Ivers-Tiffée, E. Three-Electrode Setups for Lithium-Ion Batteries I. Fem-Simulation of Different Reference Electrode Designs and Their Implications for Half-Cell Impedance Spectra. *J. Electrochem. Soc.* **2017**, *164*, A71–A79.

(21) Ender, M.; Weber, A.; Ivers-Tiffée, E. Analysis of Three-Electrode Setups for AC-Impedance Measurements on Lithium-Ion Cells by FEM Simulations. *J. Electrochem. Soc.* **2011**, *159*, A128.

(22) Williams, D. B.; Carter, C. B. *Transmission Electron Microscopy: A Textbook for Materials Science*, 2nd ed.; Springer US: Boston, MA, 2009.

(23) Pei, A.; Zheng, G.; Shi, F.; Li, Y.; Cui, Y. Nanoscale Nucleation and Growth of Electrodeposited Lithium Metal. *Nano Lett.* **2017**, *17*, 1132–1139.

(24) Qian, J.; Adams, B. D.; Zheng, J.; Xu, W.; Henderson, W. A.; Wang, J.; Bowden, M. E.; Xu, S.; Hu, J.; Zhang, J. G. Anode-Free Rechargeable Lithium Metal Batteries. *Adv. Funct. Mater.* **2016**, *26*, 7094–7102.

(25) Suzuki, S.; Ishikawa, Y.; Isshiki, M.; Waseda, Y. Native Oxide Layers Formed on the Surface of Ultra High-Purity Iron and Copper Investigated by Angle Resolved XPS. *Mater. Trans., JIM* **1997**, *38*, 1004–1009.

(26) Garnaud, G. The Formation of a Double Oxide Layer on Pure Copper. *Oxid. Met.* **1977**, *11*, 127–132.

(27) Keil, P.; Lützenkirchen-Hecht, D.; Frahm, R. Investigation of Room Temperature Oxidation of Cu in Air by Yoneda-XAFS. *AIP Conf. Proc.* **2006**, *882*, 490–492.

(28) Jiang, X.; Herricks, T.; Xia, Y. CuO Nanowires Can Be Synthesized by Heating Copper Substrates in Air. *Nano Lett.* **2002**, *2*, 1333–1338.

(29) Han, J.-W.; Lohn, A.; Kobayashi, N. P.; Meyyappan, M. Evolutional Transformation of Copper Oxide Nanowires to Copper Nanowires by a Reduction Technique. *Mater. Express* **2011**, *1*, 176–180.

(30) Poizot, P.; Laruelle, S.; Grugeon, S.; Dupont, L.; Tarascon, J. M. Nano-Sized Transition-Metal Oxides as Negative-Electrode Materials for Lithium-Ion Batteries. *Nature* **2000**, *407*, 496–499.

(31) Park, J. C.; Kim, J.; Kwon, H.; Song, H. Gram-Scale Synthesis of Cu<sub>2</sub>O Nanocubes and Subsequent Oxidation to CuO Hollow Nanostructures for Lithium-Ion Battery Anode Materials. *Adv. Mater.* **2009**, *21*, 803–807.

(32) Wang, C.; Li, Q.; Wang, F.; Xia, G.; Liu, R.; Li, D.; Li, N.; Spendlow, J. S.; Wu, G. Morphology-Dependent Performance of CuO Anodes via Facile and Controllable Synthesis for Lithium-Ion Batteries. *ACS Appl. Mater. Interfaces* **2014**, *6*, 1243–1250.

(33) Brown, Z. L.; Jurng, S.; Nguyen, C. C.; Lucht, B. L. Effect of Fluoroethylene Carbonate Electrolytes on the Nanostructure of the Solid Electrolyte Interphase and Performance of Lithium Metal Anodes. *ACS Appl. Energy Mater.* **2018**, *1*, 3057–3062.

(34) Orazem, M. E.; Tribollet, B. *Electrochemical Impedance Spectroscopy*, 2nd ed.; Wiley, 2017.

(35) La Mantia, F.; Wessells, C. D.; Deshazer, H. D.; Cui, Y. Reliable Reference Electrodes for Lithium-Ion Batteries. *Electrochem. Commun.* **2013**, *31*, 141–144.

(36) Wieczorek, W.; Florjanczyk, Z.; Stevens, J. R. Composite Polyether Based Solid Electrolytes. *Electrochim. Acta* **1995**, *40*, 2251–2258.

(37) Liu, W.; Lee, S. W.; Lin, D.; Shi, F.; Wang, S.; Sendek, A. D.; Cui, Y. Enhancing Ionic Conductivity in Composite Polymer Electrolytes with Well-Aligned Ceramic Nanowires. *Nat. Energy* **2017**, *2*, 17035.

(38) Zhang, S.; Ding, M. S.; Xu, K.; Allen, J.; Jow, T. R. Understanding Solid Electrolyte Interface Film Formation on Graphite Electrodes. *Electrochem. Solid-State Lett.* **2001**, *4*, A206.